

## Magnetic Semimetals and Quantized Anomalous Hall Effect in $\text{EuB}_6$

Simin Nie<sup>1,2</sup>, Yan Sun,<sup>3</sup> Fritz B. Prinz,<sup>2</sup> Zhijun Wang<sup>1,4,\*</sup>, Hongming Weng,<sup>1,4</sup> Zhong Fang,<sup>1,4</sup> and Xi Dai<sup>5,†</sup>


<sup>1</sup>Beijing National Laboratory for Condensed Matter Physics, and Institute of Physics, Chinese Academy of Sciences, Beijing 100190, China

<sup>2</sup>Department of Materials Science and Engineering, Stanford University, Stanford, California 94305, USA

<sup>3</sup>Max Planck Institute for Chemical Physics of Solids, Nöthnitzer Str. 40, 01187 Dresden, Germany

<sup>4</sup>University of Chinese Academy of Sciences, Beijing 100049, China

<sup>5</sup>Department of Physics, Hong Kong University of Science and Technology, Clear Water Bay, Kowloon 999077, Hong Kong

 (Received 10 August 2019; accepted 22 January 2020; published 21 February 2020)

Exploration of the novel relationship between magnetic order and topological semimetals has received enormous interest in a wide range of both fundamental and applied research. Here we predict that “soft” ferromagnetic material  $\text{EuB}_6$  can achieve multiple topological semimetal phases by simply tuning the direction of the magnetic moment. Explicitly,  $\text{EuB}_6$  is a topological nodal-line semimetal when the moment is aligned along the [001] direction, and it evolves into a Weyl semimetal with three pairs of Weyl points by rotating the moment to the [111] direction. Interestingly, we identify a composite semimetal phase featuring the coexistence of a nodal line and Weyl points with the moment in the [110] direction. Topological surface states and anomalous Hall conductivity, which are sensitive to the magnetic order, have been computed and are expected to be experimentally observable. Large-Chern-number quantum anomalous Hall effect can be realized in its [111]-oriented quantum-well structures.

DOI: [10.1103/PhysRevLett.124.076403](https://doi.org/10.1103/PhysRevLett.124.076403)

Topological semimetals (TSMs) exhibit topologically protected quasiparticles near the Fermi level ( $E_F$ ), among which Dirac fermions [1–3] and Weyl fermions [4–8] have elementary particle counterparts in high-energy physics while others (such as threefold spin-1 fermions [9–11], nodal-line fermions [12–15]) do not. These quasiparticles are classified according to the degeneracy and the shape of the band-touching points. The discrete band-touching points with fourfold (twofold) degeneracy are termed Dirac (Weyl) fermions, while the line-contact band-touching points are known as nodal-line fermions. By breaking certain crystal-line symmetry, topological nodal-line semimetals (TNLSs) can be driven into Weyl semimetals (WSMs) [16], Dirac semimetals [17,18], and topological insulators [19–21]. As we know for centrosymmetric systems with time-reversal symmetry, the band inversion (BI) between two bands with opposite parity, happening only in the small area around a single time reversal invariant momentum (TRIM), results in a TNLS or topological insulator in the absence or presence of spin-orbit coupling (SOC) without considering an additional symmetry [22–24]. However, for those with magnetic order (breaking time-reversal symmetry), this kind of BI gives rise to  $\chi = 1$  with the definition,

$$(-1)^\chi \equiv \prod_{j=\{1,2,\dots,n_{\text{occ}}\}, \Gamma_i=\text{TRIMs}} \xi_i^j, \quad (1)$$

where  $\xi_i^j$  is the parity eigenvalue of the  $j$ th band at the TRIM  $\Gamma_i$ , and  $n_{\text{occ}}$  is the total number of the occupied bands.

We note that  $\chi = 1$  implies that the system cannot be fully gapped [25,26] even with SOC. Generally speaking, it can be either a TNLS or a WSM, as shown in Fig. 1, depending on the magnetic symmetries.

Therefore, magnetic order provides us a promising way to control symmetry and topology. For example, new types

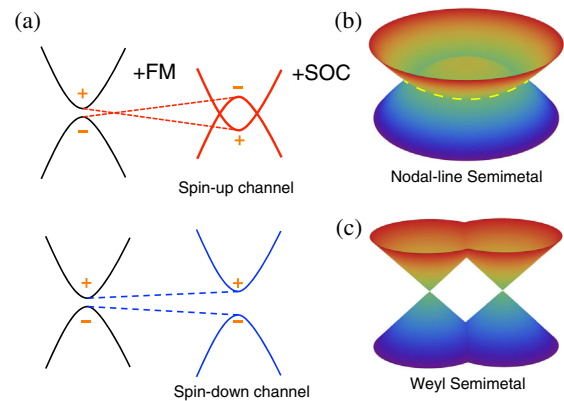


FIG. 1. Schematics of the BI with opposite exchange splitting in FM order. Starting from the narrow-gap centrosymmetric semiconductor with even-parity conduction band and odd-parity valence band, by introducing ferromagnetism, the exchange splitting pushes the spin-up valence band and spin-down conduction band upwards and downwards, respectively. This results in BI in the spin-up channel [the upper panel of (a)], but enlarges the band gap in the spin-down channel [the lower panel of (a)]. After considering SOC, the system becomes either a TNLS (b) or a magnetic WSM (c).

of Dirac semimetals are proposed to exist in antiferromagnetic materials [27,28]. Although magnetic WSMs have been predicted in some ferromagnetic (FM) materials, most of them are “hard” magnetic materials [6–8], which are difficult to manipulate with magnetic order and symmetry. In Ref. [25], Wang *et al.* proposed Weyl points (WPs) in “soft” FM alloy materials. However, alloying the sample is needed to significantly shift down the WP energy while keeping the main band structure and magnetic order unchanged, which is a big challenge for the experimental verification. Given the intense interest in the magnetic TSMs [29–31], it is important to find the stoichiometric crystals with desired topological properties and magnetic orders, providing an ideal path to overcome the above shortcomings, and study the interplay between the topological phases and tunable magnetic orders.

Over the decades, europium hexaboride ( $\text{EuB}_6$ ), a well-known soft magnetic material, has been extensively studied due to the appearance of interesting electrical transport properties near the FM transition temperatures, such as the metal-insulator transition [32,33], the giant blueshift of the unscreened plasma frequency [34,35], the large zero-bias anomalies [36], large negative magnetoresistance [32,37], etc. At  $T_{c1} = 15.3$  K [38–40], a phase transition from the paramagnetic (PM) phase to the FM phase with moment oriented to the [001] direction (called FM1) is experimentally observed in  $\text{EuB}_6$ , along with a drop of an order of magnitude in its resistivity [32]. Evidence of another phase transition from FM1 to a new FM phase with the moment oriented to the [111] direction (called FM2) is observed at  $T_{c2} = 12.5$  K [38,39]. Recent Andreev reflection spectroscopy reported that only about half of the carriers are spin polarized at the  $E_F$  [41], which seems to be in contradiction with the previous calculations suggesting a half-metallic ground state [42,43]. The incompatible results could be explained by the change of chemical potential due to the deficiencies of samples. Although there are several theoretical calculations, the exploration of the topological properties has not been reported, which might shed light on the explanation of the above electrical transport properties.

In this work, we have systematically investigated the electronic structures of  $\text{EuB}_6$  in both PM and FM phases. We show that PM  $\text{EuB}_6$  is an intrinsic semiconductor [Fig. 2(c)] with a tiny gap (about 20 meV) at three Z points (including the X, Y, and Z points), which is in good agreement with the experimental observations of the semiconductor behavior at high temperature [44]. Once the temperature is below ferromagnetic  $T_c$ , the consequent magnetic moment has opposite effective exchange splitting on the low-energy bands, leading to the BI at three Z points in the spin-up channel, but enlarging the band gap in the spin-down channel [as shown in Fig. 1(a) or Fig. 2(d)]. The BI between two opposite-parity bands resulting in  $\chi = 1$  represents an ideal toy model, guaranteeing the existence of nodal lines or odd pairs of WPs in centrosymmetric

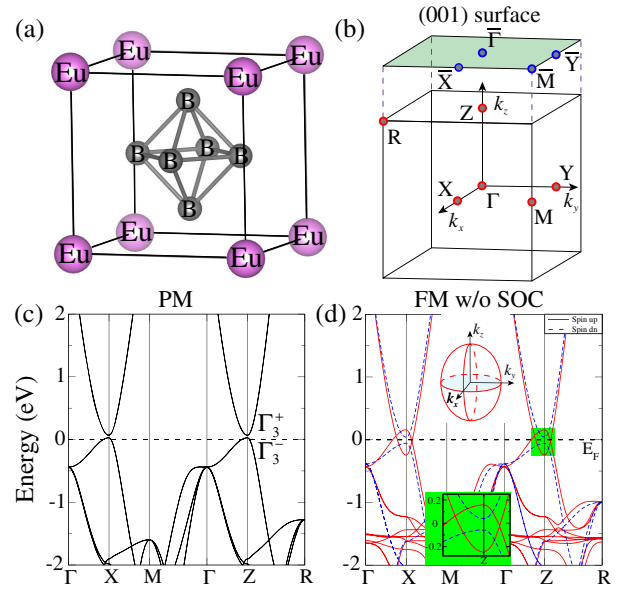


FIG. 2. Crystal structure and band structures of  $\text{EuB}_6$ . (a) Crystal structure of  $\text{EuB}_6$ . (b) The bulk and (001)-surface Brillouin zones for  $\text{EuB}_6$ . (c) Modified Becke-Johnson exchange and (d) GGA +  $U$  band structures of PM  $\text{EuB}_6$  and FM  $\text{EuB}_6$ , respectively. Upper inset: three of the five intersecting nodal lines at the Z point. Lower inset: enlargement of the band structure around the Z point. X, Y, and Z points are equivalent due to  $\hat{C}_3^{111}$  symmetry, as shown in Sec. A of Supplemental Material [45].

materials [25,26]. As expected, FM1  $\text{EuB}_6$  is a TNLs with three nodal lines (one for each Z point) protected by mirror symmetry  $\hat{M}_z$ , while it is driven into a WSM with three pairs of WPs (one pair for each Z point) in the FM2 phase. Interestingly, by rotating the magnetic moment to the [110] direction (called FM3), a composite phase with coexistence of a nodal line and WPs is found. Topological surface states and anomalous Hall conductivity (AHC) are obtained. The computed AHC suggests that FM2 and FM3 phases exhibit substantial anomalous Hall effect due to the existence of WPs, while the AHC of the FM1 phase is almost zero. In addition, large-Chern-number quantum anomalous Hall effect (QAHE) is proposed to be realized in its [111]-oriented quantum-well (QW) structures.

*The PM state in high temperature.*—At high temperature, the magnetic order is absent. Here, an “open core” treatment of Eu  $4f$  electrons has been used to treat them as core states, which have negligible effect on the bands near  $E_F$ . Considering the well-known underestimation of the band gap within generalized gradient approximation (GGA), modified Becke-Johnson exchange calculation is performed to obtain the accurate band structure along the high-symmetry lines in Fig. 2(b) (see details in Sec. B of the Supplemental Material [45]), as shown in Fig. 2(c). It shows that PM  $\text{EuB}_6$  is a semiconductor with a tiny direct gap ( $\sim 20$  meV) at three Z points, which is consistent with previous measurements [32,37,44]. Under the little group

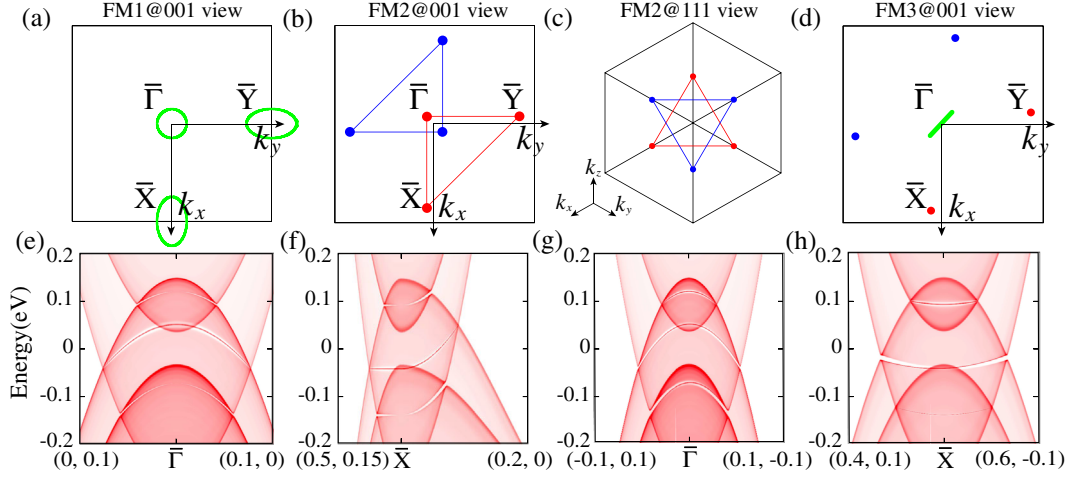


FIG. 3. Nodal lines, WPs, and surface states in FM  $\text{EuB}_6$ . The 001 view of the FM1 (a) and FM3 (d) states. The 001 view (b) and 111 view (c) of the FM2 state. The green lines represent the nodal lines. The red and blue points represent the WPs with charge 1 and -1, respectively. (e) and (f) The surface states of the FM1 phase near  $\bar{\Gamma}$  and  $\bar{X}$ , respectively. The surface states of FM2 (g) and FM3 (h)  $\text{EuB}_6$  along  $(-0.1, 0.1) - \bar{\Gamma} - (0.1, -0.1)$  and  $(0.4, 0.1) - \bar{X} - (0.6, -0.1)$  in units of  $[2\pi/a, 2\pi/a]$ , respectively.

( $D_{4h}$ ) of the Z point, the valence band and conduction band with opposite parity near  $E_F$  are labeled as  $\Gamma_3^-$  and  $\Gamma_3^+$ , respectively, playing a critical role in further study of FM  $\text{EuB}_6$ , as shown in Fig. 1.

*FM states at low temperature.*—After FM transition, all the local moments of Eu  $f^7$  configuration are aligning in the same direction. As the magnetism in  $\text{EuB}_6$  is “soft” [38], meaning that it can be easily tuned by temperature or an external magnetic field, we have first performed the calculations for the FM state without (w/o) SOC. The band structures for the spin-up (red solid lines) and spin-down (blue dashed lines) channels are shown in Fig. 2(d). The highest valence band at three Z points is mainly from an anti-bonding orbital formed by Eu  $f$  and B  $p$  states. The spin-up valence band hybridizes strongly with the occupied  $f$  states below  $E_F$ , while the hybridization shift (level repulsion) in the spin-down channel is very small and of opposite sign, since the unoccupied  $f$  bands are high above  $E_F$  due to the on-site Coulomb repulsion. As a result, we obtain an effective antiferromagnetic exchange coupling in the valence band. However, the exchange coupling of the conduction band (mainly from Eu  $d$  states) with local  $f$  states is of FM  $f$ - $d$  intra-atomic origin [43]. Therefore, the effective exchange splitting has opposite sign on the two low-energy bands. Because of this special exchange splitting, the BI happens at three Z points in the spin-up channel, while the normal band gap increases in the spin-down channel. It results in full spin polarization at  $E_F$ , consistent with previous calculations [42,43]. Although there seems to be a conflict with some experimental results showing about 50% spin-polarized states, the half-metallic state can be easily tuned into an incomplete spin-polarized state by light doping (see details in Sec. C of the Supplemental Material [45]). As most samples are electron- or hole-doped, the experimental

results may sensitively depend on the chemical potential. The experimental observations of the metallic behavior in the FM states [32,33] qualitatively support our conclusion of the BI feature. Since the correct electron correlation  $U$  is unknown and the internal parameter  $u$  slightly varies from samples to samples, we have systematically investigated the phase diagram by computing the band gaps (i.e.,  $\eta = E_{\Gamma_3^+} - E_{\Gamma_3^-}$ ) in both spin-up and spin-down channels (see details in Sec. D of the Supplemental Material [45]). The obtained phase diagram shows that the BI of the spin-up channel survives in a large area of the parameter space, indicating much promise for finding the TSM phases in  $\text{EuB}_6$ .

When SOC is ignored, the BI results in five intersecting nodal lines at the Z point protected by five mirror symmetries ( $\hat{M}_z, \hat{M}_{x/y}, \hat{M}_{110/1\bar{1}0}$ ), three of which are shown schematically in the upper inset of Fig. 2(d). Then, we include SOC in the calculations and consider three FM states with different directions of magnetization (i.e., FM1||[001], FM2||[111], and FM3||[110]). The small energy difference between them indicates that the magnetic moment can be easily tuned (see details in Sec. E of the Supplemental Material [45]). After consideration of SOC, a gap will open along the nodal lines. However, due to the BI resulting in  $\chi = 1$ , the nodal lines cannot be fully gapped out, and nodal lines or odd pairs of WPs are guaranteed around each Z point. The exact situation strongly depends on the FM direction, as will be shown below.

*Topology with different magnetic directions.*—In the case of FM1 with [001] magnetism, the symmetry reduces to the magnetic symmetry group:  $\{C_{4h} \oplus \mathcal{T}\hat{M}_x C_{4h}\}$ , where the symmetry group  $C_{4h}$  is generated by  $\hat{I}$  and  $\hat{C}_4^z$  (see details in Sec. F of the Supplemental Material

[45]). Since  $\hat{M}_z$  is still preserved and also belongs to the little group of three  $Z$  points, three nodal lines are expected, with one for each point. The calculated results are shown in Fig. 3(a). Consistently, two nodal rings (around  $X$  and  $Y$ , respectively) are found in the  $k_z = 0$  plane and one (around  $Z$ ) in the  $k_z = \pi$  plane. Because of the strong anisotropy of the band dispersion, the nodal line is oval shaped around the  $X/Y$  point, while it is almost a circle around the  $Z$  point. The  $kp$  invariant model is constructed (see more details in Sec. F of the Supplemental Material [45]) in the vicinity of each  $Z$  point, giving exactly the same band crossings as obtained from the first-principles calculations.

When the magnetic field is aligned with the [111] direction (FM2), the magnetic symmetry group becomes  $\{C_{3i} \oplus \mathcal{T}\hat{C}_2^{110}C_{3i}\}$ , where the symmetry group  $C_{3i}$  is generated by  $\hat{I}$  and  $\hat{C}_3^{111}$ . At the  $Z(X, Y)$  point,  $[\mathcal{T}\hat{C}_2^{110}(01\bar{1}, 10\bar{1})]^2 = 1$  can stabilize WPs in the  $k_x = k_y$  ( $k_y = k_z$ ,  $k_z = k_x$ ) plane. We do find a pair of WPs for each  $Z$  point. The coordinates of two WPs near the  $Z$  point are found to be  $\vec{W}_1 = [\pm 0.03978, \pm 0.03978, 0.5 \pm 0.07854]$  (hereafter, the coordinates of  $k$  points are given in units of  $[2\pi/a, 2\pi/a, 2\pi/a]$ ). The corresponding models are derived in Sec. F of the Supplemental Material [45] and yield consistent results. The other two pairs around the  $X$  and  $Y$  points are obtained by  $\hat{C}_3^{111}$  (See the exact coordinates in Sec. G of the Supplemental Material [45]). As a result, the (111) plane through the  $X$ ,  $Y$ , and  $Z$  points shown in Fig. S5(a) [45], has a nontrivial Chern number  $C = 3$ , which is crucial to realize large-Chern-number QAHE in its [111]-oriented QW structure.

When the magnetic field is aligned with the [110] direction, the symmetry reduces to the magnetic symmetry group:  $\{C_{2h} \oplus \mathcal{T}\hat{C}_2^c C_{2h}\}$ , where the symmetry group  $C_{2h}$  is generated by  $\hat{I}$  and  $\hat{C}_2^{110}$ . Interestingly, the  $Z$  point is not equivalent to the  $X/Y$  point any more. Although  $\hat{M}_z$  is broken by the [110] magnetism,  $\hat{M}_{110}$  symmetry restores. As shown in Fig. 3(d), one nodal line (shown as the green line) circled around the  $Z$  point in the  $k_x + k_y = 0$  plane still survives due to the protection of  $\hat{M}_{110}$ . However, at the  $X/Y$  point, there is no any mirror symmetry. A pair of WPs can be found in the  $k_z = 0$  plane, which are stabilized by the combined antiunitary symmetry with the relation  $[\mathcal{T}C_2^z]^2 = 1$  [57]. The coordinates of the WPs near the  $X$  point are found to be  $\vec{W}_2 = [0.5 \pm 0.06204, \pm 0.06287, 0]$ , and the WPs near the  $Y$  point can be obtained by  $\hat{C}_2^{110}$ . As expected, the (110) plane through both the  $X$  and  $Y$  points has a nonzero Chern number  $C = 2$ .

*Topological surface states and AHC.*—Topological nontrivial surface states are calculated and shown in Fig. 3. For FM1 EuB<sub>6</sub> drumhead surface states are obtained within the energy gap [Figs. 3(e) and 3(f)]. For FM2 and FM3 EuB<sub>6</sub> a chiral surface mode is obtained, as shown in Figs. 3(g)

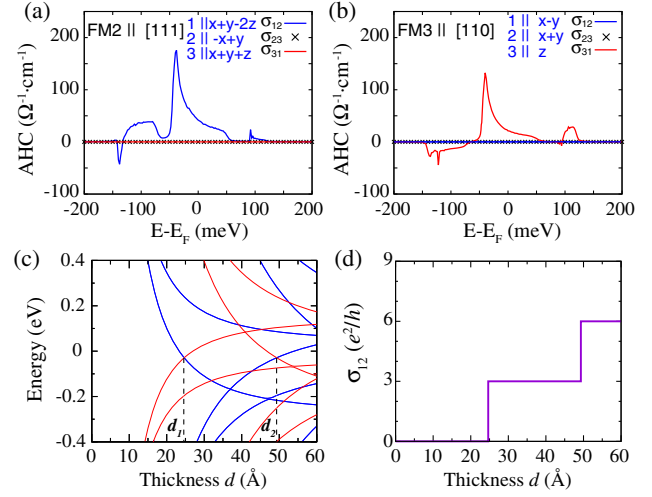


FIG. 4. AHC and quantum anomalous Hall conductivity. Energy dependent AHC of FM2 (a) and FM3 (b) EuB<sub>6</sub>. (c) The evolution of the band energies at the  $Z$  point as a function of film thickness ( $d$ ). (d) The quantized Hall conductivity as a function of the film thickness ( $d$ ).

and 3(h), respectively. The nontrivial surface states should be observable (see details in Sec. I of the Supplemental Material [45]). In addition, the anomalous Hall effect is another exotic consequence of magnetic WSM. The magnitude of AHC can be easily evaluated by  $\sigma_{xy} = (e^2/h) (\Delta k_z^W / 2\pi)$ , where  $\Delta k_z^W$  is the distance between WPs projected onto the  $z$  axis [58,59]. The calculated AHC are shown in Figs. 4(a) and 4(b) (the coordinates are redefined, with a new axis parallel to the magnetic direction), while the AHC in the FM1 phase shown in Fig. S7 [45] is almost zero near  $E_F$  [60] (see details in Sec. G of the Supplemental Material [45]). That is because of the substantial displacement of the WPs along the [111]/[110] direction in FM2/FM3 state, whereas there is no such WP displacement in the nodal line phase (i.e., FM1 state). The calculated values are relatively small. This is because (i) the band structure is complicated due to the anisotropy. Namely, the energy bands vary in an energy range from  $-0.025$  to  $0.065$  eV; (ii) the hybridizing gap is small due to the weak SOC strength. In fact, the anomalous Hall effect has been observed in the bulk magnetic EuB<sub>6</sub> [61].

*QAHE in QW structures.*—Magnetic WSM can be viewed as a stack of two-dimensional Chern insulators with strong coupling in the stacking direction. By considering its QW structure, the quantized Hall effect can be achieved due to the confinement effect, without an external magnetic field, which is also known as the QAHE [62]. Based on the effective  $kp$  models in Sec. F of the Supplemental Material [45], the Hamiltonians for the [111]-oriented QWs of FM2 EuB<sub>6</sub> have been constructed (see details in Sec. H of the Supplemental Material [45]). The evolution of the low-energy subbands at the  $Z$  point as a function of the film thickness ( $d$ ) is calculated and shown

in Fig. 4(c). When the film is very thin, the BI in the bulk FM2 EuB<sub>6</sub> is removed and the film is a trivial insulator. After the first critical thickness (about 24 Å), BI happens between a hole subband and an electron subband with even (red lines) and odd (blue lines) parity, respectively. Consequently, it leads to a jump in the Chern number or the Hall coefficient  $\sigma_{12}$  [63], as shown in Fig. 4(d). We find subsequent jumps of  $\sigma_{12}$  in unit of  $3e^2/h$ , because BI happens at the three Z points. As the thin film of EuB<sub>6</sub> has been grown successfully [64], the large-Chern-number QAHE in EuB<sub>6</sub> is experimentally realizable.

*Conclusion.*—In summary, we have studied topological phases in FM EuB<sub>6</sub> adopting first-principles calculations and effective models. In the PM phase, two bands near  $E_F$  have different parity eigenvalues at three Z points. The effective magnetic exchange splitting has opposite effect on the two bands, leading to the BI in the spin-up channel. The calculated phase diagram shows that the BI between two bands with opposite parity survives in a large region. This kind of BI guarantees the existence of either nodal lines or odd pairs of WPs. Generally speaking, even though the magnetic moment is tuned in an arbitrary direction (breaking all mirror symmetries), odd pairs of WPs are still guaranteed around each Z point. Topological surface states and AHC are obtained. We find that the AHC is sensitive to the magnetic order, which can be further measured in experiments. In the [111]-oriented QW structure of FM2 EuB<sub>6</sub>, large-Chern-number QAHE can be achieved.

S. N. and F. B. P. are supported by Volkswagen of America and the Affiliates Program of the Nanoscale Prototyping Laboratory. Z. W. is supported by the National Natural Science Foundation of China (No. 11974395), the CAS Pioneer Hundred Talents Program, and the National Thousand-Young-Talents Program. X. D. and H. M. W. are supported by the Ministry of Science and Technology of China (Grant No. 2016YFA0300600) and the K.C. Wong Education Foundation (Grant No. GJTD-2018-01). X. D. acknowledges financial support from the Hong Kong Research Grants Council (Project No. GRF16300918). This work partially used the Extreme Science and Engineering Discovery Environment, which is supported by National Science Foundation Grant No. ACI-1548562. Specifically, it used the Bridges system, which is supported by NSF Award No. ACI-1445606, at the Pittsburgh Supercomputing Center.

\* wzj@iphy.ac.cn

† daix@ust.hk

- [1] S. M. Young, S. Zaheer, J. C. Y. Teo, C. L. Kane, E. J. Mele, and A. M. Rappe, *Phys. Rev. Lett.* **108**, 140405 (2012).  
 [2] Z. Wang, Y. Sun, X.-Q. Chen, C. Franchini, G. Xu, H. Weng, X. Dai, and Z. Fang, *Phys. Rev. B* **85**, 195320 (2012).

- [3] Z. Wang, H. Weng, Q. Wu, X. Dai, and Z. Fang, *Phys. Rev. B* **88**, 125427 (2013).  
 [4] H. B. Nielsen and M. Ninomiya, *Phys. Lett.* **130B**, 389 (1983).  
 [5] L. Balents, *Physics* **4**, 36 (2011).  
 [6] X. Wan, A. M. Turner, A. Vishwanath, and S. Y. Savrasov, *Phys. Rev. B* **83**, 205101 (2011).  
 [7] G. Xu, H. Weng, Z. Wang, X. Dai, and Z. Fang, *Phys. Rev. Lett.* **107**, 186806 (2011).  
 [8] S. Nie, H. Weng, and F. B. Prinz, *Phys. Rev. B* **99**, 035125 (2019).  
 [9] B. Bradlyn, J. Cano, Z. Wang, M. Vergniory, C. Felser, R. Cava, and B. A. Bernevig, *Science* **353**, aaf5037 (2016).  
 [10] P. Tang, Q. Zhou, and S.-C. Zhang, *Phys. Rev. Lett.* **119**, 206402 (2017).  
 [11] T. Zhang, Z. Song, A. Alexandradinata, H. Weng, C. Fang, L. Lu, and Z. Fang, *Phys. Rev. Lett.* **120**, 016401 (2018).  
 [12] A. A. Burkov, M. D. Hook, and L. Balents, *Phys. Rev. B* **84**, 235126 (2011).  
 [13] C. Fang, Y. Chen, H.-Y. Kee, and L. Fu, *Phys. Rev. B* **92**, 081201(R) (2015).  
 [14] H. Weng, X. Dai, and Z. Fang, *J. Phys. Condens. Matter* **28**, 303001 (2016).  
 [15] Z.-M. Yu, W. Wu, X.-L. Sheng, Y. X. Zhao, and S. A. Yang, *Phys. Rev. B* **99**, 121106(R) (2019).  
 [16] R. Yu, Q. Wu, Z. Fang, and H. Weng, *Phys. Rev. Lett.* **119**, 036401 (2017).  
 [17] Y. Kim, B. J. Wieder, C. L. Kane, and A. M. Rappe, *Phys. Rev. Lett.* **115**, 036806 (2015).  
 [18] R. Yu, H. Weng, Z. Fang, X. Dai, and X. Hu, *Phys. Rev. Lett.* **115**, 036807 (2015).  
 [19] J.-M. Carter, V. V. Shankar, M. A. Zeb, and H.-Y. Kee, *Phys. Rev. B* **85**, 115105 (2012).  
 [20] S. Nie, G. Xu, F. B. Prinz, and S.-c. Zhang, *Proc. Natl. Acad. Sci. U.S.A.* **114**, 10596 (2017).  
 [21] S. Nie, L. Xing, R. Jin, W. Xie, Z. Wang, and F. B. Prinz, *Phys. Rev. B* **98**, 125143 (2018).  
 [22] Q. Xu, R. Yu, Z. Fang, X. Dai, and H. Weng, *Phys. Rev. B* **95**, 045136 (2017).  
 [23] H. Huang, J. Liu, D. Vanderbilt, and W. Duan, *Phys. Rev. B* **93**, 201114(R) (2016).  
 [24] S. Murakami, *New J. Phys.* **9**, 356 (2007).  
 [25] Z. Wang, M. G. Vergniory, S. Kushwaha, M. Hirschberger, E. V. Chulkov, A. Ernst, N. P. Ong, R. J. Cava, and B. A. Bernevig, *Phys. Rev. Lett.* **117**, 236401 (2016).  
 [26] T. L. Hughes, E. Prodan, and B. A. Bernevig, *Phys. Rev. B* **83**, 245132 (2011).  
 [27] P. Tang, Q. Zhou, G. Xu, and S.-C. Zhang, *Nat. Phys.* **12**, 1100 (2016).  
 [28] G. Hua, S. Nie, Z. Song, R. Yu, G. Xu, and K. Yao, *Phys. Rev. B* **98**, 201116(R) (2018).  
 [29] I. Belopolski, K. Manna, D. S. Sanchez, G. Chang, B. Ernst, J. Yin, S. S. Zhang, T. Cochran, N. Shumiya, H. Zheng *et al.*, *Science* **365**, 1278 (2019).  
 [30] D. Liu, A. Liang, E. Liu, Q. Xu, Y. Li, C. Chen, D. Pei, W. Shi, S. Mo, P. Dudin *et al.*, *Science* **365**, 1282 (2019).  
 [31] N. Morali, R. Batabyal, P. K. Nag, E. Liu, Q. Xu, Y. Sun, B. Yan, C. Felser, N. Avraham, and H. Beidenkopf, *Science* **365**, 1286 (2019).

- [32] C. Guy, S. von Molnar, J. Etourneau, and Z. Fisk, *Solid State Commun.* **33**, 1055 (1980).
- [33] P. Nyhus, S. Yoon, M. Kauffman, S. L. Cooper, Z. Fisk, and J. Sarrao, *Phys. Rev. B* **56**, 2717 (1997).
- [34] L. Degiorgi, E. Felder, H. R. Ott, J. L. Sarrao, and Z. Fisk, *Phys. Rev. Lett.* **79**, 5134 (1997).
- [35] S. Broderick, B. Ruzicka, L. Degiorgi, H. R. Ott, J. L. Sarrao, and Z. Fisk, *Phys. Rev. B* **65**, 121102(R) (2002).
- [36] B. Amsler, Z. Fisk, J. L. Sarrao, S. Von Molnar, M. W. Meisel, and F. Sharifi, *Phys. Rev. B* **57**, 8747 (1998).
- [37] S. Süllo, I. Prasad, M. C. Aronson, S. Bogdanovich, J. L. Sarrao, and Z. Fisk, *Phys. Rev. B* **62**, 11626 (2000).
- [38] S. Süllo, I. Prasad, M. C. Aronson, J. L. Sarrao, Z. Fisk, D. Hristova, A. H. Lacerda, M. F. Hundley, A. Vigliante, and D. Gibbs, *Phys. Rev. B* **57**, 5860 (1998).
- [39] M. L. Brooks, T. Lancaster, S. J. Blundell, W. Hayes, F. L. Pratt, and Z. Fisk, *Phys. Rev. B* **70**, 020401(R) (2004).
- [40] T. Fujita, M. Suzuki, and Y. Ishikawa, *Solid State Commun.* **33**, 947 (1980).
- [41] X. Zhang, S. von Molnár, Z. Fisk, and P. Xiong, *Phys. Rev. Lett.* **100**, 167001 (2008).
- [42] S. Massidda, A. Continenza, T. De Pascale, and R. Monnier, *Z. Phys. B* **102**, 83 (1996).
- [43] J. Kuneš and W. E. Pickett, *Phys. Rev. B* **69**, 165111 (2004).
- [44] J. D. Denlinger, G.-H. Gweon, S.-K. Mo, J. W. Allen, J. L. Sarrao, A. D. Bianchi, and Z. Fisk, *J. Phys. Soc. Jpn.* **71**, 1 (2002).
- [45] See Supplemental Material at <http://link.aps.org/supplemental/10.1103/PhysRevLett.124.076403> for details on the crystal structure and symmetries, calculation methods, adjustment of the spin polarization as a function of the chemical potential, Phase diagrams with varying  $U$  and  $u$ , total energies and band structures for different FM states, effective  $kp$  models, distribution of WPs and AHC for FM1  $\text{EuB}_6$ , Chern numbers of FM2  $\text{EuB}_6$  QWs, and surface states of FM  $\text{EuB}_6$ , which includes Refs. [46–56].
- [46] J. Tarascon, J. Soubeyrou, J. Etourneau, R. Georges, J. Coey, and O. Massenet, *Solid State Commun.* **37**, 133 (1981).
- [47] P. Blaha, K. Schwarz, G. Madsen, D. Kvasnicka, and J. Luitz, *WIEN2k: An Augmented Plane Wave Plus Local Orbitals Program for Calculating Crystal Properties* (TU Vienna, Vienna, 2001).
- [48] J. P. Perdew, K. Burke, and M. Ernzerhof, *Phys. Rev. Lett.* **77**, 3865 (1996).
- [49] F. Tran and P. Blaha, *Phys. Rev. Lett.* **102**, 226401 (2009).
- [50] V. I. Anisimov, I. V. Solovyev, M. A. Korotin, M. T. Czyżyk, and G. A. Sawatzky, *Phys. Rev. B* **48**, 16929 (1993).
- [51] N. Marzari, A. A. Mostofi, J. R. Yates, I. Souza, and D. Vanderbilt, *Rev. Mod. Phys.* **84**, 1419 (2012).
- [52] Q. Wu, S. Zhang, H.-F. Song, M. Troyer, and A. A. Soluyanov, *Comput. Phys. Commun.* **224**, 405 (2018).
- [53] X. Wang, J. R. Yates, I. Souza, and D. Vanderbilt, *Phys. Rev. B* **74**, 195118 (2006).
- [54] J. Kim, W. Ku, C.-C. Lee, D. S. Ellis, B. K. Cho, A. H. Said, Y. Shvyd'ko, and Y.-J. Kim, *Phys. Rev. B* **87**, 155104 (2013).
- [55] C. S. Snow, S. L. Cooper, D. P. Young, Z. Fisk, A. Comment, and J.-P. Ansermet, *Phys. Rev. B* **64**, 174412 (2001).
- [56] C. Lin and A. J. Millis, *Phys. Rev. B* **71**, 075111 (2005).
- [57] Z. Wang, D. Gresch, A. A. Soluyanov, W. Xie, S. Kushwaha, X. Dai, M. Troyer, R. J. Cava, and B. A. Bernevig, *Phys. Rev. Lett.* **117**, 056805 (2016).
- [58] A. A. Burkov and L. Balents, *Phys. Rev. Lett.* **107**, 127205 (2011).
- [59] L. Šmejkal, Y. Mokrousov, B. Yan, and A. H. MacDonald, *Nat. Phys.* **14**, 242 (2018).
- [60] J. Noky, Q. Xu, C. Felser, and Y. Sun, *Phys. Rev. B* **99**, 165117 (2019).
- [61] G. A. Wigger, R. Monnier, H. R. Ott, D. P. Young, and Z. Fisk, *Phys. Rev. B* **69**, 125118 (2004).
- [62] Y. Wang, Z. Wang, Z. Fang, and X. Dai, *Phys. Rev. B* **91**, 125139 (2015).
- [63] C.-X. Liu, X.-L. Qi, X. Dai, Z. Fang, and S.-C. Zhang, *Phys. Rev. Lett.* **101**, 146802 (2008).
- [64] R. Bachmann, K. Lee, T. Geballe, and A. Menth, *J. Appl. Phys.* **41**, 1431 (1970).